Geophysical Research Letters

RESEARCH LETTER
10.1029/2020GL087758

Shock Melting Curve of Iron: A Consensus on the Temperature at the Earth's Inner Core Boundary

HPSTAR 982-2020

Jun Li[1], Qiang Wu[1], Jiabo Li[1], Tao Xue[1], Ye Tan[1], Xianming Zhou[1], Youjun Zhang[2,3], Zhengwei Xiong[4], Zhipeng Gao[1,4], and Toshimori Sekine[3]

[1]National Key Laboratory for Shock Wave and Detonation Physics, Institute of Fluid Physics, China Academy of Engineering Physics, Mianyang, China, [2]Institute of Atomic and Molecular Physics, Sichuan University, Chengdu, China, [3]Center for High Pressure Science and Technology Advanced Research, Shanghai, China, [4]Joint Laboratory for Extreme Conditions Matter Properties, Southwest University of Science and Technology and Research Center of Laser Fusion, Mianyang, China

Key Points:
- The melting temperatures of shocked iron are measured up to ~256 GPa by the time-resolved pyrometer
- The melting curves of iron at high pressures agree with each other in dynamic and static experiments and theories
- The temperature at the inner core boundary is anchored to 5950(400) K based on the melting curve of iron

Supporting Information:
- Supporting Information S1

Correspondence to:
Y. Zhang
zhangyoujun@scu.edu.cn

Citation:
Li, J., Wu, Q., Li, J., Xue, T., Tan, Y., & Zhou, X., et al. (2020). Shock melting curve of iron: A consensus on the temperature at the Earth's inner core boundary. *Geophysical Research Letters*, *47*, e2020GL087758. https://doi.org/10.1029/2020GL087758

Received 28 MAR 2020
Accepted 18 JUL 2020
Accepted article online 23 JUL 2020

Abstract The Earth's core consists of iron as the major component. The melting point of iron at the inner core boundary constrains the thermal structure and solidification of the Earth's core. However, the current estimation of the melting temperature of iron under the core conditions has significant variations. Here, we measured the temperatures of iron shocked up to ~256 GPa using precise pyrometer and velocimeter diagnostics via a two-stage light-gas gun. Our results indicated that the melting temperatures of iron at the core-mantle and inner core boundaries are 4300(250) and 5950(400) K, respectively. These temperatures are significantly lower than some previous shock experiments but are overall consistent with the recent results determined by fast X-ray diffraction techniques, X-ray absorption experiments in laser-heated diamond anvil cells, and by ab initio computations. Our iron melting curve indicates a relatively small Clapeyron slope and supports thermal models for a young inner core.

Plain Language Summary Iron is the main constituent of the Earth's core, so its melting characteristics at high pressures are fundamentally crucial for understanding the thermal structure, solidification, and evolution of the core. We determined shock temperatures of melted iron up to ~256 GPa precisely by the use of a time-resolved quasi-spectral optical pyrometer. Our results are 1000–2000 K lower than those of some previous shock experiments. Our study reconciles the previous discrepancy in the melting temperatures of iron at pressures of 200–300 GPa and is consistent with theoretical calculations. We conclude that the melting temperature of iron at the Earth's inner core boundary is ~5950(400) K. The present study indicates a relatively gentle melting slope of iron and supports a young inner core age of ~0.565 Gyr inferred from paleomagnetic observations.

1. Introduction

Earth's core is composed of an iron alloy with a certain amount of light elements, such as Si, S, O, C, and H (Li & Fei, 2014). The melting temperatures of iron and its alloys at high pressures are critical geophysical parameters for understanding the thermal structure, inner core solidification, and energetics of the core (Kuwayama et al., 2020; Nimmo, 2015; Zhang et al., 2019). The liquid outer core and solid inner core are equilibrated at the inner core boundary (ICB, ~330 GPa), where the temperature corresponds to the melting point (Buffett, 2003). Therefore, the melting point of iron at ~330 GPa can be used to determine the adiabatic geotherm in the core. Extensive efforts have been undertaken to determine the phase diagram of iron at high pressure and temperature (P-T) using static laser-heated diamond anvil cell (DAC) techniques (e.g., Anzellini et al., 2013; Morard et al., 2018) and dynamic shock wave compressions (e.g., Brown & McQueen, 1986; Nguyen & Holmes, 2004). However, due to the difficulties in generating ultrahigh P-T conditions, measuring temperatures, and detecting melts in the experiments, the phase diagram and melting of iron at the Earth's core pressures have continued to be debated over the last 50 years. Theoretical studies also have difficulties in handling high temperatures because atoms do not follow a simple harmonic motion at high temperatures, and the electronic correlations in iron make computations more complicated (Pourovskii, 2019).

Previous studies give a range of iron melting temperatures from 5500 to 7000 K at the ICB pressure in the extrapolations of static measurements (e.g., Anzellini et al., 2013; Aquilanti et al., 2015; Morard et al.,

2018; Zhang et al., 2016), dynamic measurements (e.g., Bass et al., 1987; Harmand et al., 2015; Ping et al., 2013; Yoo et al., 1993), and theoretical calculations (e.g., Alfè, 2009; Belonoshko et al., 2000; Bouchet et al., 2013; Laio et al., 2000; Sola & Alfè, 2009; Sun et al., 2018). Under the current status of the iron phase diagram with such a considerable uncertainty, the thermal structure and evolution of the core cannot be well constrained.

Recent high P-T experiments of iron by fast X-ray diffraction (XRD) (Anzellini et al., 2013) and X-ray absorption near-edge structure (XANES) (Morard et al., 2018) in laser-heated DACs reached an agreement on iron's melting temperature up to the core-mantle boundary (CMB, at 4250(250) K and ~135 GPa). Early XANES experiments in laser-heated DACs demonstrated a low melting temperature of ~3090 K at ~103 GPa (Aquilanti et al., 2015), but their samples were likely contaminated by carbon from the diamond anvils (Morard et al., 2018). In addition, the melting experiments by synchrotron Mössbauer spectroscopy (SMS) in laser-heated DACs (Jackson et al., 2013; Zhang et al., 2016) are consistent with fast XRD and XANES experiments when the thermal pressure is corrected (Morard et al., 2018). Although recent electrical resistance measurements of iron in resistance-heated DACs indicate a lower melting temperature by ~500 K at high pressures (Sinmyo et al., 2019), the DAC works reach an overall agreement on the melting temperature of iron at the CMB pressure. At higher pressures, there are some limited data via heated DACs, and the extrapolations place the melting point of iron at the ICB from ~5500 to 6200(500) K (Anzellini et al., 2013; Sinmyo et al., 2019).

In shock wave compression experiments, sound velocity results indicate that shocked-iron starts to melt at ~220 GPa and is completely melted at ~260 GPa (Brown & McQueen, 1986; Nguyen & Holmes, 2004). The melting points of iron were then calculated to be 5600(500) K at ~243 GPa by Brown and McQueen (1986) and 5100(500) K at ~225 GPa by Nguyen and Holmes (2004), respectively, through thermodynamic calculations from the equation of state and sound velocity measurements. However, an optical pyrometer cannot directly measure the shock temperature of iron at the Hugoniot state due to its opacity. Consequently, the "sample/window" interface temperature is usually measured to derive the Hugoniot temperature of iron (Bass et al., 1987; Yoo et al., 1993). Bass et al. (1987) obtained the Hugoniot temperatures of a thin iron film or foil (0.5–10 μm thick) using an Al_2O_3 single crystal window up to ~300 GPa and deduced a melting temperature of 7800(500) K at the pressure of the ICB. Subsequently, Yoo et al. (1993) determined the Hugoniot temperatures of ~2-μm-thick iron films, sputtered onto a diamond window, up to ~340 GPa, and estimated the temperature to be 6830(500) K at the pressure of the ICB. In the previous shock temperature measurements, the optical pyrometer used only had a few channels (4–6) at wavelengths between 300 and 800 nm, which would introduce a large uncertainty with respect to the temperature determination (Anderson & Ahrens, 1996). In addition, thin iron samples used in previous studies possibly suffered from porosity (1–2% lower density than bulk iron) and an imperfect sample/window interface (an interfacial gap or surface roughness) (Tan et al., 2005; Yoo et al., 1993), which might have resulted in a false high shock temperature.

In this study, we employed bulk iron to shock compress and reach the solid-liquid phase boundary (~260 GPa) by a two-stage light-gas gun. We used a time-resolved quasi-spectral pyrometer to measure the shock temperatures at the interface between the iron and LiF transport window and simultaneously measured the particle velocity by a photon Doppler velocity (PDV) interferometer during temperature measurements. We applied thick samples and machined the sample/window interface to ideal boundary conditions and used a 16-channel optical pyrometer technique to ensure precise temperature measurements. Based on the measured temperatures and one-dimensional conduction model at the interface, the melting temperatures of iron along the Hugoniot and quasi-isentropic release were obtained when combined with the thermodynamic properties of the iron and window. Our results are lower than some previously determined melting temperatures by gas-gun shock compression but consistent with recent works by laser-heated DACs, which are well supported by ab initio computations. Our study determines the temperature at the ICB and constrains the thermal structure and evolution of the core.

2. Materials and Methods

High purity (99.98 + %) bulk iron was used as the starting material and was machined into 2.5-mm-thick disks (36 mm in diameter). The iron specimen was characterized by electron backscattered diffraction

(EBSD) through a field emission scanning electron microscope (FESEM, Carl Zeiss Supra VP55, Germany) with an operating voltage of 10 kV. The analyses show that the iron sample was fine-grained polycrystalline with a grain size of ~10–20 μm (Figure S1 in the supporting information). We performed shock experiments using a 30-mm-bore two-stage light-gas gun at the Institute of Fluid Physics, China Academy and Engineering Physics, China. Steel (304SS and HR2) was used as the flyer plates with a diameter of ~25 mm and a thickness of ~3.2 mm. Projectile velocities were measured using the optic beam break-out (OBB) method within an ~1% uncertainty, where laser-beam interruptions triggered the time interval counters. We used a transparent single-crystal LiF with [100] orientation (~30 mm in diameter and ~8 mm in thickness) as the window behind the sample (Figure S2 in the supporting information) to maintain the compression state and observe the thermal radiance at the sample/window interface. The LiF window has better optical properties and less shock-induced extinction (Liu et al., 2015) than window materials such as sapphire and diamond used in the previous studies (Yoo et al., 1993). The details of the sample characterizations and assemblage are available in the supporting information (Figures S1 and S2).

We shocked iron up to the solid-liquid mixed-phase region to obtain the melting temperatures of iron according to the previous sound velocity measurements and phase diagram of iron under shock loading (Denoeud et al., 2016; Harmand et al., 2015; Nguyen & Holmes, 2004). The shock temperature (T_H) of the mixed-phase iron is on the melting curve (T_M) at the Hugoniot pressure (P_H). A subsequent release wave, which originated after the shock wave reached the LiF window, lowered the pressure P_H to the interface pressure (P_I) due to the lower shock impedance of LiF than that of the iron sample (Lone et al., 2013). The shock pressures of iron in the present study are 196.4(3.1), 198.0(3.1), 217.3(3.3), 234.9(3.4), and 256.1(4.1) GPa, and the corresponding partially released pressures at the interface were 109.1(2.0), 110.7(2.0), 120.6(2.2), 129.0(2.3), and 141.4(2.8) GPa, respectively (Table S1 in the supporting information).

The temperature at the iron/LiF interface was measured using optical pyrometer diagnostics by recording its thermal radiation at multiple wavelengths (Li et al., 2017; Zhang et al., 2018). Our 16-wavelength optical pyrometer between 400 and 800 nm ensures high accuracy in the fitting analysis. The photomultiplier tube (PMT) channel in the pyrometer with a narrow bandwidth filter of 10-nm-spectral-width had a high time resolution of ~3 ns (Zhou et al., 2015). Before carrying out the experiments, each channel was calibrated by the spectral radiance from a tungsten-halogen lamp (WBr) as the high-temperature blackbody standard (Lyzenga & Ahrens, 1980). Digital oscilloscopes with a sampling rate of 2 GHz recorded the pyrometer outputs. The method details can be found in our previous work (Zhang et al., 2018).

Radiant spectra were obtained from a 16-core silica fiber probe in the pyrometer measurements (Figure 1a). Point A indicates the shock wave arrival at the iron/LiF interface, which maintains a compressed state until the arrival of a rarefaction wave, as Point B shows (Figure 1a). A typical fitting of the spectral radiance versus wavelength to Planck's equation in iron at an interface pressure of ~109.1 GPa is shown in Figure 1b and others are shown in Figure S3 in the supporting information. The fitted temperature (T_I) and emissivity (ε) values for the shocked iron are listed in Table S2 in the supporting information. Although the fitting to the gray body model introduces uncertainties to the fitted value, it is the preferred method to determine radiation temperatures of 3000–10000 K by an optical pyrometer in the visible spectrum range.

The particle velocity profile (u_{pi}) at the interface measured by the PDV simultaneously shows a clear plastic single-wave structure (Figure 1c). The shock Hugoniot states of iron in this study were obtained by the Rankine-Hugoniot equations and the impedance matching method (Table S1 in the supporting information). The interface pressure, P_I, was directly determined from the measured particle velocity of LiF. A typical particle velocity and a temperature profile at ~109.1 GPa are plotted as a function of time in Figure 1d. The temperature profile showed a spike peak of ~350 K during the first 10–30 ns corresponding to the shock wave arrival at Time A (Figures 1a). The subsequent profile maintained a nearly constant value to reach Time B (Figure 1d), demonstrating that the shock-induced flash from the interfacial residual gas was effectively minimized in our experiments. It is thus believed that the interface was close to the ideal contact and reached physical thermal equilibrium under shock compression.

The temperature profiles in Shots No. Fe01 to Fe04 exhibit stable plateaus between Times A and B, except for the spike peaks (Figures 1d and S4 in the supporting information). However, in Shot No. Fe05 at the highest interface pressure of ~141.4 GPa, it showed a gradual decrease with time during compression (Figure S4 in the supporting information). This decrease could be explained by the endothermic melting reaction of the

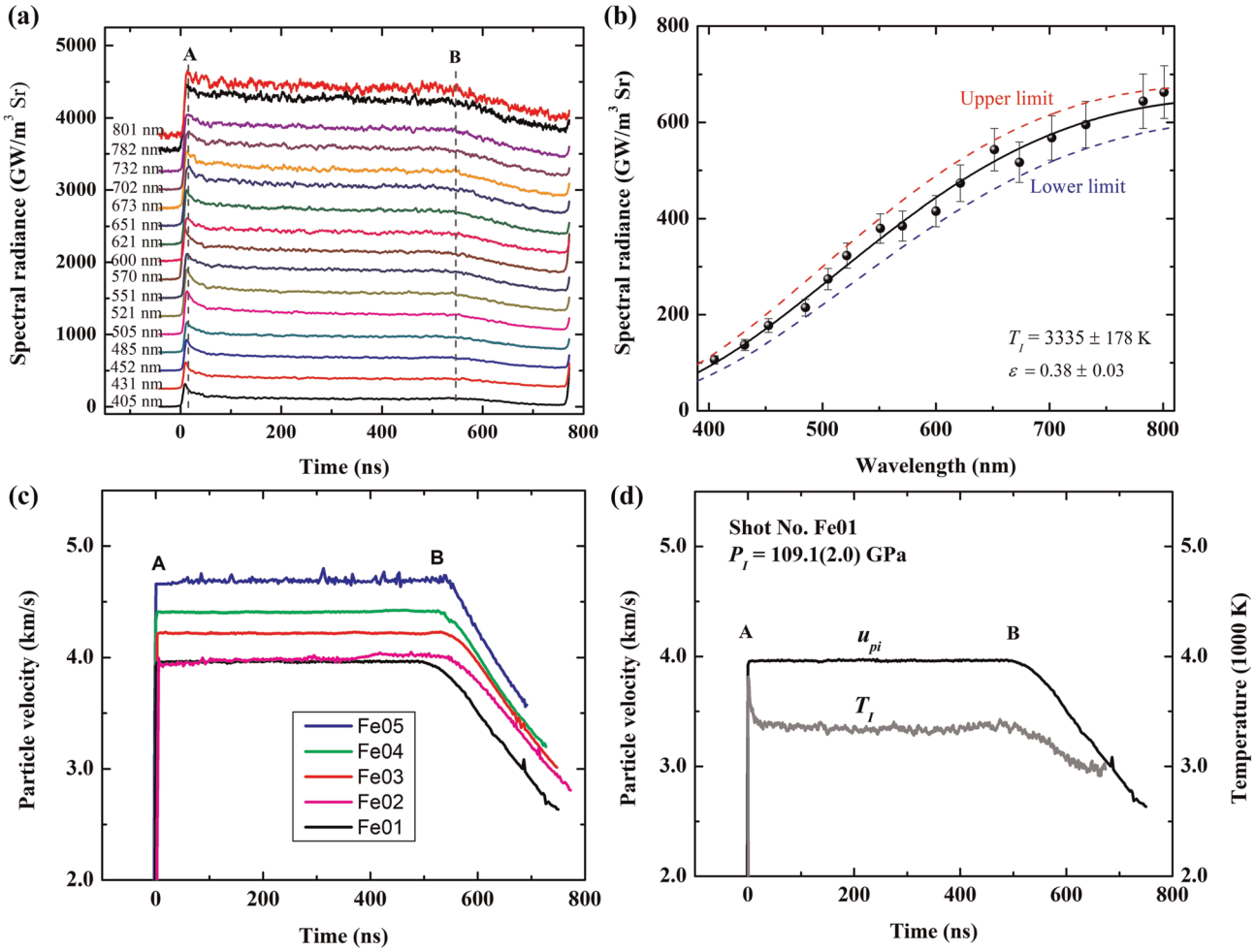

Figure 1. Spectral radiance and particle velocity measured at the interface of iron/LiF. Typical spectral radiance profiles measured by a 16-channel time-resolved optical pyrometer (a) and the fitted curve to determine the temperature and emissivity of iron (b) in Shot No. Fe01. Particle velocity profiles at the iron/LiF interface as a function of time measured by PDV in Shots No. Fe01 to Fe05 (c), and a comparison of the profiles between the time-revolved particle velocity (u_{pi}) and interfacial temperature (T_I) in Shot No. Fe01 (d).

LiF window because LiF melts above ~134 GPa (Liu et al., 2015). A similar phenomenon was also observed in the shock temperature measurements of an Fe-Ni-Si alloy (Zhang et al., 2018). Three shots at pressures between 217 and 256 GPa are considered to be located on the melting curve of iron because the shock conditions are within the field indicated by the previous sound velocity measurements (Figure 2a) (Brown & McQueen, 1986; Nguyen & Holmes, 2004).

3. Results

3.1. Shock Temperatures of Iron

The measured T_I is lower than the temperature of iron (T_R) at the interface because thermal conduction at the iron/LiF interface occurs from iron to LiF at P_I. We used a one-dimensional thermal conduction model (Grover model) to obtain the temperature in iron at the interface (Grover & Urtiew, 1974; Yoo et al., 1993):

$$T_R = T_I + (T_I - T_W)/\alpha \tag{1}$$

$$\alpha = \left[\frac{(\rho C\kappa)_S}{(\rho C\kappa)_W}\right]^{1/2} \tag{2}$$

where T_W is the LiF window temperature at P_I and ρ, C, and κ represent the density, heat capacity, and thermal conductivity, respectively, for the sample (subscript: S) and window (subscript: W). A key point

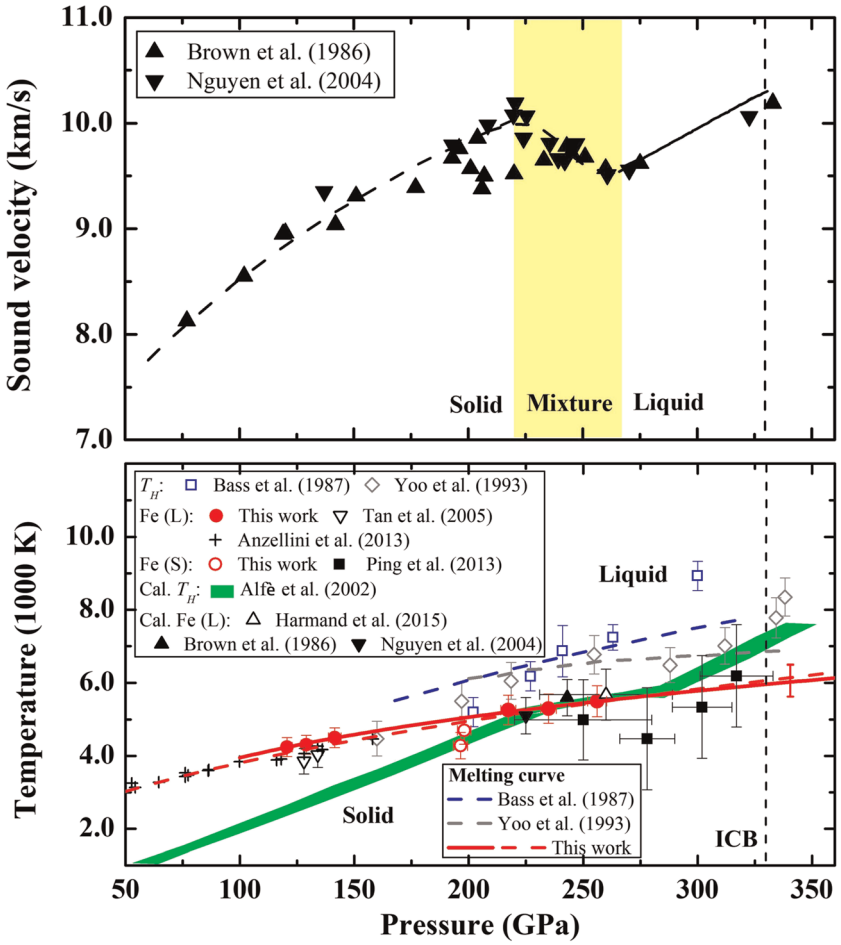

Figure 2. Experimental data on the shock melting of pure iron at high pressures. (top) Shock-induced melting of iron was indicated by a sharp decrease in the measured longitudinal sound velocity at pressures between 220 and 260 GPa (Brown & McQueen, 1986; Nguyen & Holmes, 2004). (bottom) The measured temperatures at the Hugoniot and partially released states in this work are compared with the previous results by gas gun, laser shock, laser-heated DACs, and theoretical calculations. The open and solid red circles represent the measured temperatures for solid iron and iron on the melting curve. The blue and gray dashed lines represent the melting curve of iron based on the previous shock Hugoniot temperature measurements on iron foil and/or film by Bass et al. (1987) (marked by open blue squares) and Yoo et al. (1993) (marked by open gray diamonds), respectively. The open black inverted triangles represent the temperatures at the iron film/LiF interface measured by a pyrometer with six channels in a two-stage light-gas gun (Tan et al., 2005). The solid black triangles (Brown & McQueen, 1986) and inverted triangles (Nguyen & Holmes, 2004) represent the thermodynamically calculated melting temperatures of iron from the equation of state and sound velocity measurements by gas-gun shock. The open black triangle represents the calculated temperature of liquid iron produced by single laser shock compression combined with SOP and XANES diagnostics (Harmand et al., 2015). The solid black squares represent the modeled shock temperatures of *hcp*-iron at off-Hugoniot states under multiple laser shock compression (Ping et al., 2013). Crosses represent the melting points of iron by fast XRD in laser-heated DACs (Anzellini et al., 2013). The solid and dashed red lines are the melting curves evaluated from the Simon-Glatzel law in this work. The green belt represents the Hugoniot temperature-pressure of iron calculated by the ab initio method with upper and lower bounds for the calculations without and with free-energy correction, respectively (Alfè et al., 2002). T_H is the Hugoniot temperature of iron; the L and S indicate the liquid and solid-states of iron, respectively.

to obtain the temperature T_R is the thermophysical parameters of related materials at high pressure. We used the thermal conductivities of *hcp*-iron (Xu et al., 2018; Zhang et al., 2020) and a LiF window (Liu et al., 2015; Smirnov, 2011; Zhao et al., 2014) at high pressures and temperatures determined by recent experiments and calculations (Table S2 in the supporting information). The Hugoniot density and shock temperature of single-crystal LiF were determined by previous experiments and calculations (Liu et al., 2015; Myint et al., 2019). The specific heat capacity of LiF used in this study was ~1,638 J/kg K (Andersson & Backstrom, 1987), and it was modeled as the summation of the lattice heat capacity (3*R*,

R is the gas constant) and the electronic heat capacity of shocked-iron (Brown & McQueen, 1986). Based on the thermophysical parameters, the parameter "α" in shocked iron/LiF was then calculated to be approximately 3.4–4.6. Our results show that T_R is ~300 K higher than the directly measured T_I at the interface pressure P_I (Table S2 in the supporting information).

The release process from the initial Hugoniot state is quasi-isentropic, and T_H can be obtained from T_R at the interface by a Mie-Grüneisen thermal equation:

$$T_H = T_R \exp\left[-\int_{V_R}^{V_H} (\gamma/V) dV\right] \quad (3)$$

where V_R and V_H are the volumes of iron at P_I and P_H, respectively, and γ is the thermophysical Grüneisen parameter of *hcp*-iron at high P-T taken from previous studies (Figure S5 in the supporting information) (Brown & McQueen, 1986; Dorogokupets et al., 2017; Huang et al., 2005; Sha & Cohen, 2010). The relationship among T_H, T_R, and T_I in shocked metals and alloys is illustrated in Figure S6a (Nellis & Yoo, 1990; Zhang et al., 2018). Our determined Hugoniot temperatures at pressures between 196 and 256 GPa are 1000–1500 K lower than the previous measurements by Bass et al. (1987) and Yoo et al. (1993) (Figure 2b and Table S2 in the supporting information). At the highest pressure of 256.1(4.1) GPa, our measured Hugoniot temperature was ~5498(441) K. This value is consistent overall with the Hugoniot temperature of 5680(700) K at ~260(29) GPa under laser shock compression (open triangle, Figure 2b), where the iron was in a liquid state as indicated by X-ray absorption (XANES) and the temperature was calculated by hydrodynamic simulations from a velocity interferometer system for any reflector (VISAR) or streaked optical pyrometer (SOP) measurement (Harmand et al., 2015). The determined temperatures of iron at the solid-liquid boundary are reasonably higher than the previously modeled temperatures of *hcp*-iron at the off-Hugoniot states by extended X-ray absorption fine structure spectroscopy (EXAFS) under multiple laser shock compressions (solid black squares, Figure 2) (Ping et al., 2013). Our T_H for iron in the solid and liquid states agrees well with the theoretical computations by ab initio free energy techniques (green belt, Figure 2b) (Alfè et al., 2002). We should note that the thermal conductivity of iron at high P-T reaches an agreement between recent experiments and density functional theory (DFT) calculations (Xu et al., 2018; Zhang et al., 2020). However, it is still worth considering the effect of a varied thermal conductivity of iron on our derived Hugoniot temperatures (Williams, 2018). We used the lower and upper limits of the thermal conductivity of *hcp*-iron from previous works (Konôpková et al., 2016; Ohta et al., 2016) and derived the Hugoniot temperatures correspondingly (Table S3 in the supporting information). Our results show that by varying the thermal conductivity of *hcp*-iron at high P-T by a factor of 5–6 (from 40 to 200 W/m/K) can introduce an extra uncertainty of 100–200 K in our determined Hugoniot temperatures. The determination of the Hugoniot temperatures of iron is not greatly affected by the uncertainty of its thermal conductivity, but this needs to be further investigated in future work.

3.2. Melting Curve of Iron at High Pressures

Iron is initially located in the solid-liquid mixed-phase region at shock pressures between 217 and 256 GPa, so its T_H equals T_M. Upon the partial release to the iron/LiF impedance pressure, iron remains in the melting region at the released temperature T_R due to the latent heat of fusion (Lone et al., 2013). With the thermal conduction between T_R and T_W at the interface, a subsequent solidification is introduced at T_I and P_I because T_W is significantly lower than T_R (Dai et al., 2009). The solution to the heat conduction equation with the boundary conditions across the sample/window interface can constrain the melting temperature of iron (Figure S6 in the supporting information), which is described in detail elsewhere (Tan & Ahrens, 1990; Tan et al., 2005). Therefore, we investigated the melting temperature of iron at the interface pressure from the measured interface temperature T_I. The melting temperature is located between T_I and T_R at the impedance pressure by Tan-Ahrens' model (Tan & Ahrens, 1990) as follows:

$$T_M = T_I - [(T_I - T_W) erf(\mu)]/\alpha \quad (4)$$

where $erf(\mu)$ is the error function related to the heat diffusivity of the sample, which is considered between −1 and 0 (Dai et al., 2009). As T_I is higher than T_W in our experiments (Table S2 in the supporting information), the melting temperature is approximated when erf(μ) is taken as −0.5 (Dai et al., 2009):

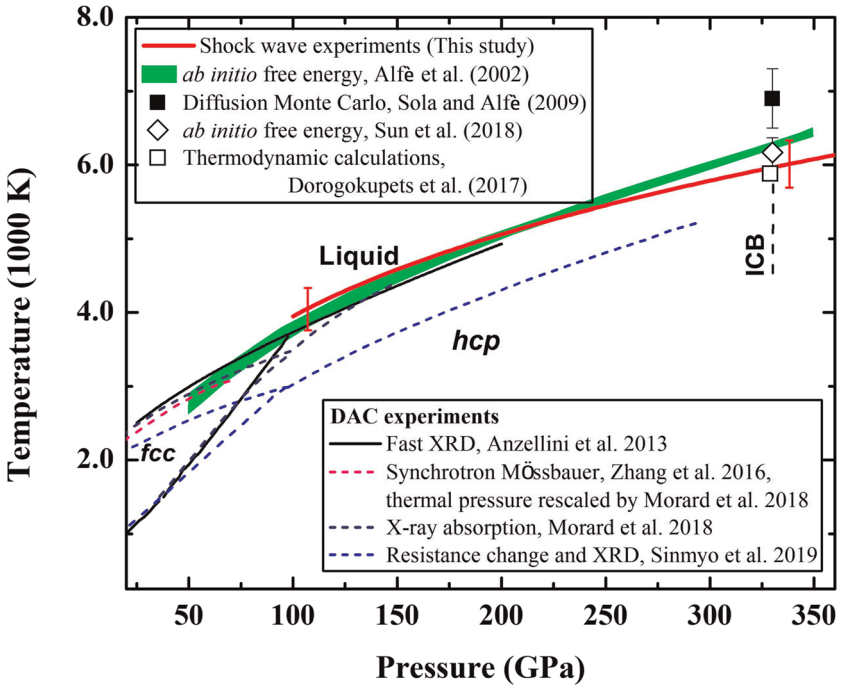

Figure 3. Melting curve of iron determined under shock loading in this work, in comparison with the previous studies by heated DACs and theoretical calculations. The melting of iron in heated DACs is identified with the results of fast XRD (solid black line) (Anzellini et al., 2013), synchrotron Mössbauer spectroscopy with a thermal pressure correction (SMS, pink dashed line) (Morard et al., 2018; Zhang et al., 2016), X-ray absorption spectra at the iron K-edge (XANES, navy dashed line) (Morard et al., 2018), and electrical resistance measurements (blue dashed line) (Sinmyo et al., 2019). The green belt represents theoretical computations by ab initio techniques with upper and lower bounds for the calculations without and with free-energy correction, respectively (Alfè et al., 2002). The melting temperature of *hcp*-iron at the ICB pressure was calculated by using the ab initio free energy calculation (open diamond) (Sun et al., 2018), the diffusion Monte Carlo method (solid square) (Sola & Alfè, 2009), and a thermodynamic model based on the Helmholtz free energy equation (open square) (Dorogokupets et al., 2017).

$$T_m \cong T_I + (T_I - T_W)/(2\alpha) = (T_I + T_R)/2 \tag{5}$$

Because $(T_I - T_W)/2\alpha$ is much smaller than temperature T_I, the determined melting temperature T_M at the interface is only 100–200 K higher than the observed interface temperature T_I (Table S2 in the supporting information). The melting points in this study at pressures between 120 and 141 GPa agree with the static experiments by fast XRD in the laser-heated DACs (Anzellini et al., 2013) (Figure 2b). The present melting temperatures at the interface pressure are 300–400 K higher than the shock results by Tan et al. (2005). The reasons for this are mainly explained by (1) the older pyrometer had only six channels with discrete wavelengths, which might introduce a large uncertainty for the temperature determination, and (2) Tan et al. (2005) approximated the measured interface temperature to be the melting temperature of iron at the interface pressure; however, it is actually lower than the melting temperature due to the thermal conduction at the interface (Figure S6 in the supporting information).

We fitted the melting points at high pressures using the semiempirical Simon-Glatzel law (Figure 2b), which describes the relationship between the melting temperature and pressure:

$$T_m = T_0 \left(\frac{P - P_0}{a} + 1 \right)^{\frac{1}{b}} \tag{6}$$

where $a = 98(15)$ and $b = 3.35(0.50)$ are empirical parameters fitted from our measured melting points between 120 and 256 GPa when taking the starting melting point $T_0 = 4242$ K at a reference pressure of $P_0 = 120.6$ GPa (solid red curve, Figure 2b); or $a = 23(2)$ and $b = 2.26(0.11)$ are fitted from both static and present shock experiments between 50 and 256 GPa when taking $T_0 = 1811$ K at ambient pressure

(red dashed curve, Figure 2b). The melting curves give ~4300(250) K to the melting point of iron at the CMB pressure (~135 GPa). The extrapolation to the ICB pressure (~330 GPa) is ~5950(400) K, which is consistent with the early thermodynamic estimates of 5800(500) K at 330 GPa by Brown and McQueen (1986) but is 1000–2000 K lower than the measurements in the shock experiments by Bass et al. (1987) and Yoo et al. (1993) (Figure 2b).

4. Discussion

Compared with previous works, our results are generally consistent with the results between 100 and 200 GPa in laser-heated DACs by fast XRD (Anzellini et al., 2013), XANES (Morard et al., 2018) and SMS (with thermal pressure rescaled) (Morard et al., 2018; Zhang et al., 2016) within experimental errors (Figure 3). These four consistent results provide the precise determination of the melting temperatures of iron up to the CMB pressure. However, a recent study observing the changes in the electrical resistance of iron with increasing temperature at high pressures in resistance-heated DACs shows a systematically lower melting temperature (blue dashed line, Figure 3) (Sinmyo et al., 2019). Further studies may need to interpret this discrepancy, but it could come from the melting kinetics, such as the preferred orientation and texture in *hcp*-iron upon heating or the reorientation of crystals in the partial melting of iron (Anzellini et al., 2013), which may affect its electrical resistance. For example, the electrical resistivity of *hcp*-iron shows anisotropy between the *a* and *c* axes at high P-T by DFT calculations (Xu et al., 2018). Therefore, the resistance may change during the fast-recrystallization of *hcp*-iron upon heating. Our determined melting point of 5950(400) K in iron at the ICB pressure is consistent with ab initio free energy calculations (6200(200) K) (Alfè et al., 2002; Sun et al., 2018) and a thermodynamic model based on the Helmholtz free energy equation (5882 K) (Dorogokupets et al., 2017) but lower than the results from diffusion Monte Carlo free energy calculations (6900(400) K).

The Clapeyron slope (dT_M/dP) of the iron melting curves (Figure 2b) can be obtained as 11.8(0.8) K/GPa at ~135 GPa (CMB pressure) and 6.6(1.0) K/GPa at ~330 GPa (ICB pressure) according to our fitted Simon-Glatzel equation. The results indicate that the slope of the melting curves gradually decreases with increasing pressure, and the value at the ICB conditions is lower than the extrapolation from the laser-heated DAC experiments by fast XRD (~9.2 K/GPa at ~330 GPa) (Anzellini et al., 2013).

The compression duration in our gas-gun shock experiments was ~500 ns (Figure 1) and was much shorter than that in heated DACs (usually a few minutes) (Anzellini et al., 2013). The agreement regarding the melting temperature of iron at high pressures by shock and static compressions further proves that thermal equilibrium was quickly established in the shocked iron. This finding is also supported by theories and experiments where the relaxation times after lattice excitations are less than a picosecond (10^{-12} s) for electrons and phonons in metals (Li et al., 2017; Siwick et al., 2003). Shock-induced superheating of iron was proposed to explain the discrepancy between the measured melting temperature by shock compression and thermodynamic calculations. It was believed that iron may be heated by shock compression at a higher heating rate than that required for the rearrangement of atoms, resulting in the melting of iron possibly being suppressed above its melting temperature (Luo & Ahrens, 2004). Our experiments show that superheating may not be significant in shocked iron because the discrepancy in the melting curve of iron is due to the large uncertainty of the previous shock temperature measurements.

The presence of light elements (such as Si, S, O, and C) in the core can actually depress the melting temperature depending on the element(s). Extrapolations of the melting data in the Fe-light element systems to the ICB conditions indicate that Fe-Si alloys may melt above 5500 K (Komabayashi et al., 2019; Zhang et al., 2018) and that Fe-O, Fe-S, and Fe-C alloys likely melt at lower temperatures of 4000–5000 K (Mashino et al., 2019; Mori et al., 2017). An iron alloy with 4–6 wt% Si, which satisfies the density deficit of the inner core, melts at 5600–5800 K at the ICB pressure (Komabayashi et al., 2019; Komabayashi, Pesce, Sinmyo, et al., 2019; Zhang et al., 2018), which can be used to constrain the adiabat of the core. Taking a constant Grüneisen parameter of 1.5 within the core (Anderson & Isaak, 2002), a temperature of 4150(200) K at the CMB (~135 GPa) is given by an adiabatic gradient model ($T = T_{ICB}(\rho/\rho_{ICB})^{\gamma}$) (Dziewonski & Anderson, 1981).

The inner core age (T_{ic}) can be constrained based on the ratio of the Clapeyron slope to the adiabat (dT_M/dT_{ad}) and the thermal conductivity of the inner core (κ) by a simplified equation (Deguen & Cardin, 2011):

$$T_{ic} < \rho_{ic} C_p \frac{r_{ic}^2}{6\kappa}\left(\frac{dT_M}{dT_{ad}} - 1\right) \quad (7)$$

where r_{ic} and ρ_{ic} are the present radius (1,221 km) and density (~13,000 kg/m^3) of the inner core (Dziewonski & Anderson, 1981), respectively, and C_p is the heat capacity of iron at the core conditions (~800 J/kg/K) (Deguen et al., 2013). A representative value for the adiabatic gradient is ~5.4 K/GPa at the ICB (Buffett, 2010). Compared with our determined melting gradient of iron at the ICB (~6.6(1.0) K/GPa), we find that its Clapeyron slope is comparable to the adiabatic gradient ($dT_M/dT_{ad} \approx 1.22(0.12)$) at the ICB. The thermal conductivity of *hcp*-iron was determined to be ~147 W/m/K under the relevant P-T condition of the ICB (~305 GPa and 6000 K) by using recent computations and experiments (Xu et al., 2018; Zhang et al., 2020), and it is located between the previous low (below ~40 W/mK; Konôpková et al., 2016; Stacey & Loper, 2007) and high (above ~200 W/mK; Ohta et al., 2016) estimates. Both the small ratio of the Clapeyron slope to the adiabat and the large thermal conductivity of iron suggest a young inner core age. The inner core age is constrained to be younger than ~0.4(0.2) Gyr for a pure iron core based on the physical properties of iron, although it strongly depends on the final determination of the thermal conductivity of iron under the ICB conditions. Light elements in the core indeed decrease the thermal conductivity of iron, and it is still likely over ~100 W/mK for an iron alloy inner core (Gomi et al., 2016; Gomi & Yoshino, 2018; Williams, 2018), which corresponds to an inner core younger than ~0.6(0.3) Gyr. Even with a thermal conductivity as low as ~40 W/mK under the ICB conditions indicated by Konôpková et al. (2016), the inner core age is unlikely to be older than ~1.5 Gyr if the small ratio of the melting slope of iron to the adiabat is applied. Our suggested inner core age is generally consistent with a recent estimate (~0.565 Gyr) inferred from the Ediacaran ultralow geomagnetic field intensity (Bono et al., 2019).

Conclusions

We measured the shock temperatures of pure iron using a time-resolved quasi-spectral optical pyrometer in a two-stage light-gas gun and determined its melting temperatures up to ~256 GPa. Our Hugoniot temperatures of iron are 1000–2000 K lower than some previous shock experiments (Bass et al., 1987; Yoo et al., 1993) but consistent with ab initio calculations (Alfè et al., 2002). The obtained melting curve of iron overall reaches a consensus between the static and dynamic compressions (Anzellini et al., 2013; Morard et al., 2018), indicating that thermal equilibrium can be quickly established in shocked iron. The current melting curve of iron indicates a melting temperature of ~5950(400) K at the ICB, which agrees with most of the recent theories (Alfè, 2009; Dorogokupets et al., 2017; Sun et al., 2018). Our study suggests that the inner core is most likely younger than ~0.57 Gyr constrained by the melting curve gradient and the recently determined thermal conductivity of iron at the ICB. In conclusion, the present study further clarifies the melting temperatures of iron at the relevant P-T condition of the core, which is important for a better understanding of the thermal structure and evolution of the Earth's core.

Data Availability Statement

Data sets for the measured spectral radiances and interface particle velocities in shocked-iron are available at the link (https://data.4tu.nl//download/uuid:c8aebb9e-1d71-49f0-99f0-303f907fb1be/).

Acknowledgments

The authors acknowledge Huayun Geng for the constructive comments and Ke Jin, Qiming Wang, and Jung-Fu Lin for the helpful discussions. We thank Suhua Ye, Xiaolong Zeng, Jin Huang, Qiang Kang, Haifeng Xuan, Shi Dong, and Feng Xi for their assistance in the pyrometer and PDV measurements. We thank Freyja O'Toole who read our manuscript and made constructive comments. This work was performed under the Science Challenge Project (TZ2016001) and the National Key Laboratory of Shock Wave and Detonation Physics (JCKYS2018212002 and 6142A03182006) and partially supported by the National Natural Science Foundation of China (U1930124 and 41804082) and the CAEP Foundation (2018AB02).

References

Alfè, D. (2009). Temperature of the inner-core boundary of the Earth: Melting of iron at high pressure from first-principles coexistence simulations. *Physical Review B*, *79*(6). https://doi.org/10.1103/PhysRevB.79.060101

Alfè, D., Price, G., & Gillan, M. (2002). Iron under Earth's core conditions: Liquid-state thermodynamics and high-pressure melting curve from ab initio calculations. *Physical Review B*, *65*(16) 165118. https://doi.org/10.1103/PhysRevB.65.165118

Anderson, O., & Isaak, D. (2002). Another look at the core density deficit of Earth's outer core. *Physics of the Earth and Planetary Interiors*, *131*(1), 19–27. https://doi.org/10.1016/S0031-9201(02)00017-1

Anderson, W. W., & Ahrens, T. J. (1996). Shock temperature and melting in iron sulfides at core pressures. *Journal of Geophysical Research*, *101*(B3), 5627–5642. https://doi.org/10.1029/95JB01972

Andersson, S., & Backstrom, G. (1987). Thermal conductivity and heat capacity of single-crystal LiF and CaF2 under hydrostatic pressure. *Journal of Physics C: Solid State Physics*, *20*(35), 5951. https://doi.org/10.1088/0022-3719/20/35/011

Anzellini, S., Dewaele, A., Mezouar, M., Loubeyre, P., & Morard, G. (2013). Melting of iron at Earth's inner core boundary based on fast X-ray diffraction. *Science*, *340*(6131), 464–466. https://doi.org/10.1126/science.1233514

Aquilanti, G., Trapananti, A., Karandikar, A., Kantor, I., Marini, C., Mathon, O., et al. (2015). Melting of iron determined by X-ray absorption spectroscopy to 100 GPa. *Proceedings of the National Academy of Sciences of the United States of America*, *112*(39), 12042–12045. https://doi.org/10.1073/pnas.1502363112

Bass, J. D., Svendsen, B., & Ahrens, T. J. (1987). The temperature of shock compressed iron. In M. H. Manghnani, & Y. Syono (Eds.), *High-pressure research in mineral physics: A volume in honor of Syun-iti Akimoto*, *Geophysical Monograph Series* (Vol. 39, pp. 393–402).Tokyo: Terra Scientific Publishing Company (TERRAPUB). https://doi.org/10.1029/GM039p0393

Belonoshko, A. B., Ahuja, R., & Johansson, B. (2000). Quasi-ab initio molecular dynamic study of Fe melting. *Physical Review Letters*, *84*(16), 3638–3641. https://doi.org/10.1103/PhysRevLett.84.3638

Bono, R. K., Tarduno, J. A., Nimmo, F., & Cottrell, R. D. (2019). Young inner core inferred from Ediacaran ultra-low geomagnetic field intensity. *Nature Geoscience*, *12*(2), 143–147. https://doi.org/10.1038/s41561-018-0288-0

Bouchet, J., Mazevet, S., Morard, G., Guyot, F., & Musella, R. (2013). Ab initio equation of state of iron up to 1500 GPa. *Physical Review B*, *87*(9) 094102. https://doi.org/10.1103/PhysRevB.87.094102

Brown, J. M., & McQueen, R. G. (1986). Phase transitions, Grüneisen parameter, and elasticity for shocked iron between 77 GPa and 400 GPa. *Journal of Geophysical Research*, *91*(B7), 7485–7494. https://doi.org/10.1029/JB091iB07p07485

Buffett, B. A. (2003). The thermal state of Earth's core. *Science*, *299*(5613), 1675–1677. https://science.sciencemag.org/content/sci/299/5613/1675.full.pdf, https://doi.org/10.1126/science.1081518

Buffett, B. A. (2010). Onset and orientation of convection in the inner core. *Geophysical Journal International*, *179*(2), 711–719. https://doi.org/10.1111/j.1365-246X.2009.04311.x

Dai, C., Hu, J., & Tan, H. (2009). Hugoniot temperatures and melting of tantalum under shock compression determined by optical pyrometry. *Journal of Applied Physics*, *106*(4), 043519. https://doi.org/10.1063/1.3204941

Deguen, R., Alboussiere, T., & Cardin, P. (2013). Thermal convection in Earth's inner core with phase change at its boundary. *Geophysical Journal International*, *194*(3), 1310–1334. https://doi.org/10.1093/gji/ggt202

Deguen, R., & Cardin, P. (2011). Thermochemical convection in Earth′s inner core. *Geophysical Journal International*, *187*(3), 1101–1118. https://doi.org/10.1111/j.1365-246X.2011.05222.x

Denoeud, A., Ozaki, N., Benuzzi-Mounaix, A., Uranishi, H., Kondo, Y., Kodama, R., et al. (2016). Dynamic X-ray diffraction observation of shocked solid iron up to 170 GPa. *Proceedings of the National Academy of Sciences of the United States of America*, *113*(28), 7745–7749. https://www.pnas.org/content/pnas/113/28/7745.full.pdf, https://doi.org/10.1073/pnas.1512127113

Dorogokupets, P. I., Dymshits, A. M., Litasov, K. D., & Sokolova, T. S. (2017). Thermodynamics and equations of state of iron to 350 GPa and 6000 K. *Scientific Reports*, *7*(1), 41,863. https://doi.org/10.1038/srep41863

Dziewonski, A. M., & Anderson, D. L. (1981). Preliminary reference Earth model. *Physics of the Earth and Planetary Interiors*, *25*(4), 297–356. https://doi.org/10.1016/0031-9201(81)90046-7

Gomi, H., Hirose, K., Akai, H., & Fei, Y. (2016). Electrical resistivity of substitutionally disordered hcp Fe-Si and Fe-Ni alloys: Chemically-induced resistivity saturation in the Earth's core. *Earth and Planetary Science Letters*, *451*, 51–61. http://www.sciencedirect.com/science/article/pii/S0012821X16303594, https://doi.org/10.1016/j.epsl.2016.07.011

Gomi, H., & Yoshino, T. (2018). Impurity resistivity of fcc and hcp Fe-based alloys: Thermal stratification at the top of the core of super-earths. *Frontiers in Earth Science*, *6*, 217. https://doi.org/10.3389/feart.2018.00217

Grover, R., & Urtiew, P. A. (1974). Thermal relaxation at interfaces following shock compression. *Journal of Applied Physics*, *45*(1), 146–152. https://doi.org/10.1063/1.1662949

Harmand, M., Ravasio, A., Mazevet, S., Bouchet, J., Denoeud, A., Dorchies, F., et al. (2015). X-ray absorption spectroscopy of iron at multimegabar pressures in laser shock experiments. *Physical Review B*, *92*(2) 024108, 024108. https://doi.org/10.1103/PhysRevB.92.024108

Huang, H.-J., Jing, F.-Q., Cai, L.-C., & Bi, Y. (2005). Grüneisen parameter along Hugoniot and melting temperature of ε-iron: A result from thermodynamic calculations. *Chinese Physics Letters*, *22*(4), 836–838. https://doi.org/10.1088/0256-307X/22/4/016

Jackson, J. M., Sturhahn, W., Lerche, M., Zhao, J., Toellner, T. S., Alp, E. E., et al. (2013). Melting of compressed iron by monitoring atomic dynamics. *Earth and Planetary Science Letters*, *362*, 143–150. http://www.sciencedirect.com/science/article/pii/S0012821X12006747, https://doi.org/10.1016/j.epsl.2012.11.048

Komabayashi, T., Pesce, G., Morard, G., Antonangeli, D., Sinmyo, R., & Mezouar, M. (2019). Phase transition boundary between fcc and hcp structures in Fe-Si alloy and its implications for terrestrial planetary cores. *American Mineralogist*, *104*(1), 94–99. https://doi.org/10.2138/am-2019-6636

Komabayashi, T., Pesce, G., Sinmyo, R., Kawazoe, T., Breton, H., Shimoyama, Y., et al. (2019). Phase relations in the system Fe-Ni-Si to 200 GPa and 3900 K and implications for Earth's core. *Earth and Planetary Science Letters*, *512*, 83–88. http://www.sciencedirect.com/science/article/pii/S0012821X19300883, https://doi.org/10.1016/j.epsl.2019.01.056

Konôpková, Z., McWilliams, R. S., Gómez-Pérez, N., & Goncharov, A. F. (2016). Direct measurement of thermal conductivity in solid iron at planetary core conditions. *Nature*, *534*(7605), 99–101. https://doi.org/10.1038/nature18009

Kuwayama, Y., Morard, G., Nakajima, Y., Hirose, K., Baron, A. Q. R., Kawaguchi, S. I., et al. (2020). Equation of state of liquid iron under extreme conditions. *Physical Review Letters*, *124*(16), 165,701. https://doi.org/10.1103/PhysRevLett.124.165701

Laio, A., Bernard, S., Chiarotti, G., Scandolo, S., & Tosatti, E. (2000). Physics of iron at Earth's core conditions. *Science*, *287*(5455), 1027–1030. https://doi.org/10.1126/science.287.5455.1027

Li, J., & Fei, Y. (2014). Experimental constraints on core composition. In K. K. Turekian (Ed.), *Treat. Geochem* (second ed.pp. 527–557). Oxford: Elsevier.

Li, J., Wu, Q., Xue, T., Geng, H., Yu, J., Jin, K., et al. (2017). The α-γ-ε triple point and phase boundaries of iron under shock compression. *Journal of Applied Physics*, *122*(2), 025901. https://doi.org/10.1063/1.4993581

Li, R., Ashour, O. A., Chen, J., Elsayed-Ali, H. E., & Rentzepis, P. M. (2017). Femtosecond laser induced structural dynamics and melting of Cu (111) single crystal. An ultrafast time-resolved x-ray diffraction study. *Journal of Applied Physics*, *121*(5) 055102. https://doi.org/10.1063/1.4975198

Liu, Q., Zhou, X., Zeng, X., & Luo, S. N. (2015). Sound velocity, equation of state, temperature and melting of LiF single crystals under shock compression. *Journal of Applied Physics*, *117*(4), 045901. https://doi.org/10.1063/1.4906558

Lone, B. M. L., Stevens, G. D., Turley, W. D., Holtkamp, D. B., Iverson, A. J., Hixson, R. S., & Veeser, L. R. (2013). Release path temperatures of shock-compressed tin from dynamic reflectance and radiance measurements. *Journal of Applied Physics*, *114*(6), 063506. https://doi.org/10.1063/1.4817764

Luo, S.-N., & Ahrens, T. J. (2004). Shock-induced superheating and melting curves of geophysically important minerals. *Physics of the Earth and Planetary Interiors*, *143–144*, 369–386. http://www.sciencedirect.com/science/article/pii/S003192010400069X

Lyzenga, G. A., & Ahrens, T. J. (1980). Shock temperature measurements in Mg_2SiO_4 and SiO_2 at high pressures. *Geophysical Research Letters*, *7*(2), 141–144. https://doi.org/10.1029/GL007i002p00141

Mashino, I., Miozzi, F., Hirose, K., Morard, G., & Sinmyo, R. (2019). Melting experiments on the Fe-C binary system up to 255 GPa: Constraints on the carbon content in the Earth's core. *Earth and Planetary Science Letters*, *515*, 135–144. http://www.sciencedirect.com/science/article/pii/S0012821X19301682, https://doi.org/10.1016/j.epsl.2019.03.020

Morard, G., Boccato, S., Rosa, A. D., Anzellini, S., Miozzi, F., Henry, L., et al. (2018). Solving controversies on the iron phase diagram under high pressure. *Geophysical Research Letters*, *45*, 11,074–11,082. https://doi.org/10.1029/2018GL079950

Mori, Y., Ozawa, H., Hirose, K., Sinmyo, R., Tateno, S., Morard, G., & Ohishi, Y. (2017). Melting experiments on Fe-Fe_3S system to 254 GPa. *Earth and Planetary Science Letters*, *464*, 135–141. http://www.sciencedirect.com/science/article/pii/S0012821X17300894

Myint, P. C., Shi, E. L., Hamel, S., Cynn, H., Jenei, Z., Lipp, M. J., et al. (2019). Two-phase equation of state for lithium fluoride. *The Journal of Chemical Physics*, *150*(7), 074506. https://doi.org/10.1063/1.5079758

Nellis, W., & Yoo, C. (1990). Issues concerning shock temperature measurements of iron and other metals. *Journal of Geophysical Research*, *95*(B13), 21,749–21,752. https://doi.org/10.1029/JB095iB13p21749

Nguyen, J. H., & Holmes, N. C. (2004). Melting of iron at the physical conditions of the Earth's core. *Nature*, *427*(6972), 339–342. https://doi.org/10.1038/nature02248

Nimmo, F. (2015). Energetics of the core. In G. Schubert (Ed.), *Treat. Geophys* (second ed., Vol. 8, pp. 27–55). Oxford: Elsevier.

Ohta, K., Kuwayama, Y., Hirose, K., Shimizu, K., & Ohishi, Y. (2016). Experimental determination of the electrical resistivity of iron at Earth's core conditions. *Nature*, *534*(7605), 95–98. https://doi.org/10.1038/nature17957

Ping, Y., Coppari, F., Hicks, D. G., Yaakobi, B., Fratanduono, D. E., Hamel, S., et al. (2013). Solid iron compressed up to 560 GPa. *Physical Review Letters*, *111*(6), 065501. https://doi.org/10.1103/PhysRevLett.111.065501

Pourovskii, L. V. (2019). Electronic correlations in dense iron: From moderate pressure to Earth's core conditions. *Journal of Physics: Condensed Matter*, *31*(37) 373001. https://doi.org/10.1088/1361-648X/ab274f

Sha, X., & Cohen, R. E. (2010). First-principles thermal equation of state and thermoelasticity of hcp Fe at high pressures. *Physical Review B*, *81*(9) 094105. https://doi.org/10.1103/PhysRevB.81.094105

Sinmyo, R., Hirose, K., & Ohishi, Y. (2019). Melting curve of iron to 290 GPa determined in a resistance-heated diamond-anvil cell. *Earth and Planetary Science Letters*, *510*, 45–52. https://doi.org/10.1016/j.epsl.2019.01.006

Siwick, B. J., Dwyer, J. R., Jordan, R. E., & Miller, R. J. D. (2003). An atomic-level view of melting using femtosecond electron diffraction. *Science*, *302*(5649), 1382–1385. https://science.sciencemag.org/content/sci/302/5649/1382.full.pdf, https://doi.org/10.1126/science.1090052

Smirnov, N. A. (2011). Ab initio calculations of the thermodynamic properties of LiF crystal. *Physical Review B*, *83*(1) 014109. https://doi.org/10.1103/PhysRevB.83.014109

Sola, E., & Alfè, D. (2009). Melting of iron under Earth's core conditions from diffusion Monte Carlo free energy calculations. *Physical Review Letters*, *103*(7), 078501. https://doi.org/10.1103/PhysRevLett.103.078501

Stacey, F. D., & Loper, D. E. (2007). A revised estimate of the conductivity of iron alloy at high pressure and implications for the core energy balance. *Physics of the Earth and Planetary Interiors*, *161*(1–2), 13–18. http://www.sciencedirect.com/science/article/pii/S0031920106003323, https://doi.org/10.1016/j.pepi.2006.12.001

Sun, T., Brodholt, J. P., Li, Y., & Vočadlo, L. (2018). Melting properties from ab initio free energy calculations: Iron at the Earth's inner-core boundary. *Physical Review B*, *98*(22) 224301. https://doi.org/10.1103/PhysRevB.98.224301

Tan, H., & Ahrens, T. J. (1990). Shock temperature measurements for metals. *High Pressure Research*, *2*(3), 159–182. https://doi.org/10.1080/08957959008201036

Tan, H., Dai, C., Zhang, L., & Xu, C. (2005). Method to determine the melting temperatures of metals under megabar shock pressures. *Applied Physics Letters*, *87*(22) 221905. https://doi.org/10.1063/1.2043248

Williams, Q. (2018). The thermal conductivity of Earth's core: A key geophysical parameter's constraints and uncertainties. *Annual Review of Earth and Planetary Sciences*, *46*(1), 47–66. https://doi.org/10.1146/annurev-earth-082517-010154

Xu, J., Zhang, P., Haule, K., Minar, J., Wimmer, S., Ebert, H., & Cohen, R. (2018). Thermal conductivity and electrical resistivity of solid iron at Earth's core conditions from first-principles. *Physical Review Letters*, *121*(9), 096601. https://doi.org/10.1103/PhysRevLett.121.096601

Yoo, C. S., Holmes, N. C., Ross, M., Webb, D. J., & Pike, C. (1993). Shock temperatures and melting of iron at Earth core conditions. *Physical Review Letters*, *70*(25), 3931–3934. https://doi.org/10.1103/PhysRevLett.70.3931

Zhang, D., Jackson, J. M., Zhao, J., Sturhahn, W., Alp, E. E., Hu, M. Y., et al. (2016). Temperature of Earth's core constrained from melting of Fe and $Fe_{0.9}Ni_{0.1}$ at high pressures. *Earth and Planetary Science Letters*, *447*, 72–83. https://doi.org/10.1016/j.epsl.2016.04.026

Zhang, Y., Hou, M., Liu, G., Zhang, C., Prakapenka, V. B., Greenberg, E., et al. (2020). Reconciliation of experiments and theory on transport properties of iron and the geodynamo. *arXiv: 2004. 12035*. https://arxiv.org/abs/2004.12035

Zhang, Y., Nelson, P., Dygert, N., & Lin, J.-F. (2019). Fe alloy slurry and a compacting cumulate pile across Earth's inner-core boundary. *Journal of Geophysical Research: Solid Earth*, *124*, 10,954–10,967. https://doi.org/10.1029/2019JB017792

Zhang, Y., Sekine, T., Lin, J.-F., He, H., Liu, F., Zhang, M., et al. (2018). Shock compression and melting of an Fe-Ni-Si alloy: Implications for the temperature profile of the Earth's core and the heat flux across the core-mantle boundary. *Journal of Geophysical Research: Solid Earth*, *123*, 1314–1327. https://doi.org/10.1002/2017JB014723

Zhao, W.-G., Zhou, X.-M., Li, J.-B., Li, J., & Zeng, X.-L. (2014). Thermal conductivity of shocked LiF single crystal measurement by liquid sandwich method. *Journal of Atomic and Molecular Physics*, *31*, 140–148.

Zhou, X., Nellis, W. J., Li, J., Li, J., Zhao, W., Liu, X., et al. (2015). Optical emission, shock-induced opacity, temperatures, and melting of $Gd_3Ga_5O_{12}$ single crystals shock-compressed from 41 to 290 GPa. *Journal of Applied Physics*, *118*(5), 055903. https://doi.org/10.1063/1.4928081